International Journal of Hydrogen Energy 135 (2025) 339–350

Contents lists available at ScienceDirect

International Journal of Hydrogen Energy

journal homepage: www.elsevier.com/locate/he

A novel flow field design for the thermal management in planar solid oxide fuel cell

Jiaxuan Wu [a], Jingjin Hu [a], Zhengkai Tu [a], Run Hu [a,b,*]

[a] School of Energy and Power Engineering, Huazhong University of Science and Technology, Wuhan 430074, China
[b] Department of Applied Physics, Kyung Hee University, Yongin-si, Gyeonggi-do 17104, Republic of Korea

ARTICLE INFO

Handling Editor: Fanglin F. Chen

Keywords:
Planar solid oxide fuel cell
Thermal management
Flow field
Temperature gradient
Pressure drop

ABSTRACT

Solid oxide fuel cell (SOFC) is recognized as a promising solution for hydrogen-based energy systems, yet its operational stability is hindered by thermal stress induced by uneven temperature distribution. In this study we propose a novel flow field configuration named the loop-flow field and analyze the thermal and flow performance. Detailed modeling and simulations are presented and compared with three typical flow fields. The results show that the maximum temperature gradient is reduced by 50.86 % compared to the cross-flow configuration. In addition, branch channels are incorporated and the influence of different branch channel widths is analyzed. The results reveal that the width of 1.5 mm optimally balances electrochemical performance and system efficiency, reducing pump power consumption by 11.1 % while simultaneously enhancing thermal performance. This loop-flow field configuration offers a notable pathway for enhancing SOFC durability and system efficiency.

1. Introduction

As a clean, efficient, and abundant energy carrier, hydrogen energy has garnered significant attention in the development of sustainable energy systems [1–4]. In hydrogen energy applications, SOFC is regarded as the promising fuel cell technology [5,6]. SOFCs are high-temperature electrochemical devices that transform hydrogen or hydrocarbon fuel chemical energy into electricity, with their operating temperature typically ranging between 600 °C and 1000 °C. It possesses advantages including low emissions, high efficiency, and easy fuel availability [7–9]. These distinctive advantages position SOFC as one of the effective solutions for achieving the clean utilization of energy.

Despite the inherent advantages mentioned above, SOFC encounter persistent limitations in maintaining optimal performance during extended operation [10,11]. A critical factor contributing to the decline of SOFC performance is the thermal stress, which arises from the high temperature gradient within the fuel cell [12–14]. Due to the different coefficients of thermal expansion of materials within the SOFC, temperature changes cause uneven expansion or contraction between materials, generating thermal stress [15]. The thermal stress can lead to material deformation, cracks, or even fractures during SOFC operation. If the thermal stress is excessive, it may compromise the structural integrity of the cell, causing electrolyte cracking, seal failure, or performance degradation, thereby shortening the SOFC's lifespan [16–18]. Local overheating will exacerbate the deterioration of SOFC component performance, or even irreversible damage [19]. Additionally, it is crucial to minimize the pressure drops across the flow field in order to reduce the power consumption of the fuel pump, which will influence the efficiency of the system [20]. Therefore, enhancing the temperature distribution and flow uniformity of SOFCs are effective approaches to improve their stability and efficiency.

The thermal-electrochemical coupling characteristics in planar SOFCs are significantly influenced by the flow configuration, as modifying the flow channel structure enhances the SOFC electrochemical performance [21,22]. Kong et al. [23] reported a novel design of X-type interconnector and evaluated against the traditional architectures. Their numerical simulations revealed the design enhances gas transport, reduces the current path and improves SOFC performance. Moreover, the effect is particularly pronounced when the cathode conductivity is low. Yan et al. [24] also reported a spiral interconnector and carried out numerical simulation and experimental verification. The results showed that the structure elevated gas velocity in the electrode, which enhanced the species transport efficiency and the fuel utilization of the SOFC. Liu et al. [25] studied the impact of different flow channel inlet shapes on the thermoelectric performance of SOFCs fueled by ammonia. The result showed that the performance of the oval-section channel was superior to

* Corresponding author. School of Energy and Power Engineering, Huazhong University of Science and Technology, Wuhan 430074, China.
E-mail address: hurun@hust.edu.cn (R. Hu).

https://doi.org/10.1016/j.ijhydene.2025.04.463
Received 7 March 2025; Received in revised form 20 April 2025; Accepted 26 April 2025
Available online 8 May 2025

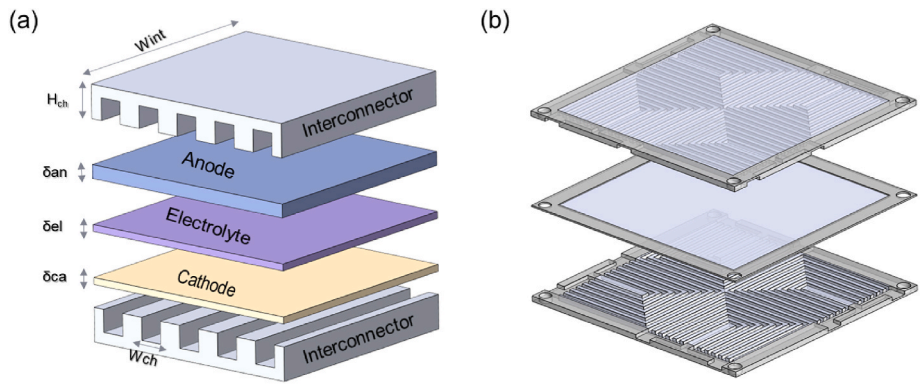

Fig. 1. (a) Geometric structure of a SOFC single cell; (b) Schematic of the loop-flow field.

the trapezoidal and triangular channels. In addition, artificial intelligence is also used to optimize the flow field structure [26]. Hao et al. [27] demonstrated that placing a separator in the fuel channel of a tubular solid oxide fuel cell effectively reduces the temperature gradient across the cell. Fu et al. [28] developed a new type of connected cable-type channel. It can effectively improve the output power of the cell. Chen et al. [29] developed a new 3D electrochemical multi-physics framework of SOFC stacks for the parallel cylindrical flow field, and compared with traditional parallel flow field. Their analysis demonstrated superior current density and reactant distribution relative to traditional configurations.

Generally, increasing the air flow can diminish the temperature gradient within SOFCs, thereby enhancing the thermal performance. However, this requires additional pump power to drive the increased air flow. Several researchers have investigated the SOFC flow arrangement to explore their impact on thermal performance. They found that improving flow uniformity [30] leads to a more uniform temperature distribution [31,32]. Three principal flow configurations — co-flow, counter-flow, and cross-flow — are operationally used in SOFC stack [33]. The co-flow configurations demonstrate superior thermal homogeneity compared to other configurations [14]. The counter-flow arrangement, despite achieving the highest temperature, provides the superior electrical properties [34]. Lu et al. [35] improved the flow field structure on the basis of the original Z-shaped flow field, and adopted the double outlet design of " one inlet and two outlets" configuration. The design achieves the best flow uniformity and a more uniform gas distribution. Gong et al. [36] proposed a ridge-optimized thermal management strategy for SOFCs achieves temperature uniformity improvements across Z/U/L flow fields via genetic algorithm.

Parametric optimization of manifold architectures serves as a pivotal determinant in the design of the external flow field [37–39]. Zhao et al. [40] integrated computational and experimental analyses reveal that inlet geometry adjustments in external manifold SOFC stacks enhance flow uniformity, while outlet modifications prioritize pressure loss reduction. Kim et al. [41] designed a four-cell SOFC stack with external manifold types and investigated its flow and thermal phenomena and properties. Bi et al. [42] evaluated planar SOFC stacks with multi-cell configurations, demonstrating that the outlet-to-inlet manifold width ratio critically governs flow uniformity. The external manifold stack architecture has been validated in planar intermediate-temperature SOFC [43]. A bottom-access structure stack for easy installation of the external manifold stack is developed by Chen et al. [44]. In addition, Gong et al. [45] implemented a bypass-valve thermal management strategy in a multi-stack configuration, achieving complete mitigation of 60 K thermal differentials through flow redistribution. They also proposed an innovative flow field architecture which reduces the temperature gradient compared to conventional designs [46], but the simulation structure thickness adopted exhibit deviations from practical industrial-scale implementations. While the above researches have demonstrated improved electrical performance by partial thermal improvements through flow field structure modifications, further improvements are needed in the design of flow fields to achieve optimal thermal management and enhance overall system efficiency.

In this study, an innovative loop-flow field is proposed to improve the temperature uniformity of SOFC. The thermal and flow properties are compared with those of three conventional flow fields. The results show that the temperature gradient is 50.86 % lower compared to the cross-flow field, with the most uniform temperature distribution. In addition, branch channels are incorporated into the loop-flow field to reduce the pressure drop. Different channel widths are compared, leading to the identification of the optimal width. The pressure drop is reduced by 11.1 %, while thermal performance is also improved. This flow field design offers a viable approach to ensuring prolonged SOFC durability and system efficiency under high-temperature conditions.

Nomenclature

Abbreviation		η_{ohm}	Ohmic overpotential(V)
SOFC/s	Solid oxide fuel cell/s	η_{conc}	Concentration overpotential (V)
3D	Three dimensional	P	Pressure (Pa)
TPB	Triple phase boundary	i_0	Reference exchange current density (A/m^2)
TD	Temperature difference	α	Transfer coefficient
PEN	Positive electrolyte negative	F	Faraday constant (C/mol)
DTD	Dimensionless temperature difference	k	Permeability of the porous medium
STD	Standard deviation	u	velocity (m/s)
PI	Performance index	Ψ	Viscous stress tensor (cSt)
TG	Temperature gradient	x_j	mole fraction
		j	Gas-phase species
Symbols		ω	Mass fraction
Φ	potential(V)	k_d	Reference diffusivity (m^2/s)
σ	Electrical conductivity (S/m)	M_i	molar mass (g/mol)
ρ	density (kg/m^3)	v_i	Diffusion volume (m^3/s)
T	Temperature(K)	k_{eff}	Effective thermal conductivity (W/(m·K))
E^o	Electromotive force at standard pressure(V)	C_p	Specific heat (J/(kg·K))
E^{ocv}	Open circuit voltage(V)	Q	Source term
η_{act}	Activation overpotential(V)		

2. Modeling

2.1. Geometric model

A three-dimensional model of a typical planar SOFC single cell is presented in Fig. 1(a), which consists of interconnects, electrodes, gas channels, and the electrolyte. Fig. 1(b) shows the SOFC single cell with an innovative loop-flow. The upper and lower structures represent interconnects, while the middle section comprises the electrolyte and electrode. Unlike conventional configurations, the loop-flow field is partitioned into four areas, featuring a symmetrical multi-inlet/multi-

Table 1
Parameters for geometric model.

parameter	value
Gas channel height, H_{ch} (mm)	1
Gas channel width, W_{ch} (mm)	1
Anode thickness, δ_{an} (μm)	300
Electrolyte thickness, δ_{el} (μm)	50
Cathode thickness, δ_{ca} (μm)	50
Interconnector height, H_{int} (mm)	1.5
Interconnector width, W_{int} (mm)	50
Interconnector length, L_{int} (mm)	50

outlet arrangement. The anode and cathode flow channels are designed with orthogonal rotational symmetry. Fuel and air enter through four lateral inlets and flows radially inward before exiting through symmetrically distributed outlets. The geometric parameters are defined in Table 1, which is based on the thickness structure of actual industrial applications.

There are three main flow fields in the typical planar SOFC single cell, which are co-flow field, cross-flow field and counter-flow field, as shown in Fig. 2(a)–(c). Fig. 2(d) presents the innovative loop-flow field. The operating conditions are the same in all cases except that the flow arrangement is different. The governing equations for momentum conservation, mass transport, and thermal energy transfer are integrated with the kinetic models governing electrochemical reactions in the electrodes.

2.2. Governing equations

2.2.1. Electrochemical model

Electrochemical charge transfer in SOFCs involves electron conduction through external circuits coupled with ionic migration across the electrolyte. Cathodic oxygen undergoes reduction to form oxygen ions, which subsequently transport through the electrolyte membrane, facilitating hydrogen oxidation at the anode-electrolyte interface. The governing equations for electron and ion transport in the fuel cell can be described as Eqs. (1)–(4) [47]:

Electrolyte:

$$\nabla \cdot i_l = Q_l \tag{1}$$

$$i_l = -\sigma_l \nabla \phi_l \tag{2}$$

Electrode:

$$\nabla \cdot i_s = Q_s \tag{3}$$

$$i_s = -\sigma_s \nabla \phi_s \tag{4}$$

where Q is the general source term, Φ is the potential, and σ is the electrical conductivity. The cell different parts of the material conductivity are different, which can be calculated as:

$$\sigma_{l,el} = 3.34 \times 10^4 \cdot \exp\left(\frac{-103000}{T}\right) \tag{5}$$

$$\sigma_{s,c} = \frac{4.2 \times 10^7}{T} \cdot \exp\left(\frac{-1200}{T}\right) \tag{6}$$

$$\sigma_{s,a} = \frac{9.5 \times 10^7}{T} \cdot \exp\left(\frac{-1150}{T}\right) \tag{7}$$

The open-circuit or reversible Nernst voltage of any fuel cell is the theoretical maximum voltage the cell can achieve under a specific set of operating conditions. During SOFC operation, the cell encounters hurdles in overcoming electrochemical limitations and internal resistance caused by ohmic losses. Additionally, dynamic changes in reactant gas concentrations induce three primary polarization effects—activation polarization, ohmic polarization, and concentration polarization—within the cell. These collective polarization losses reduce the operational voltage below the theoretical open-circuit value, as

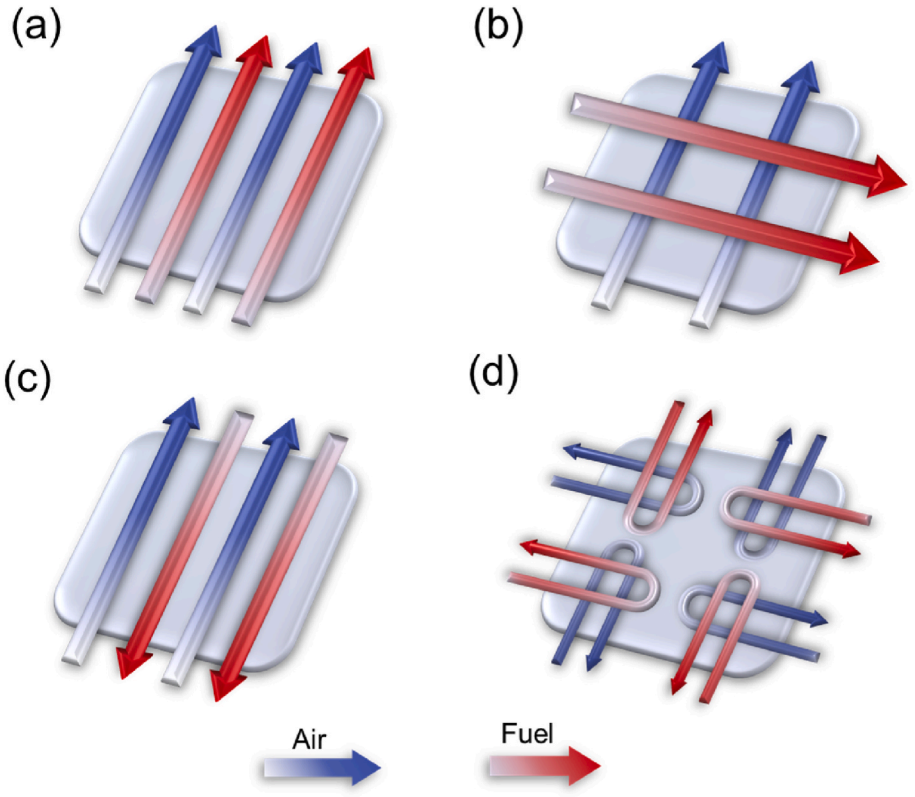

Fig. 2. Schematics of various flow field configurations: (a)Co-flow field; (b)Cross-flow field; (c)Counter-flow field; (d)Loop-flow field.

quantified by the relationship [48]:

$$E = E^{ocv} - |\eta_{act}| - \eta_{ohm} - \eta_{conc} \tag{8}$$

$$E^{ocv} = E^{o} - \frac{RT}{n_e F}\ln\left(\frac{P_{H_2O,TPB}}{P_{H_2,TPB}\sqrt{P_{O_2,TPB}}}\right) \tag{9}$$

$$E^{o} = 1.317 - 2.769 \times 10^{-4} T \tag{10}$$

where E^{o} is the electromotive force at standard pressure, E^{ocv} is the open circuit voltage, P is the partial pressure at the Triple Phase Boundary (TPB), η_{act} is the activation overpotential, η_{ohm} is the ohmic overpotential, and η_{conc} is the concentration overpotential. The activation polarizations in the electrodes are described as follows:

$$\eta_{act,a} = \phi_s - \phi_l \tag{11}$$

$$\eta_{act,c} = \phi_s - \phi_l - E^{ocv}_{H_2/O_2} \tag{12}$$

The ohmic overpotential is proportional to the current density as given by:

$$\eta_{\mathrm{ohm}} = iR_{ohm} \tag{13}$$

where R_{ohm} is the is the internal resistance of the cell, as given by

$$R_{ohm} = \frac{\tau_{anode}}{\sigma_{anode}} + \frac{\tau_{electrolyte}}{\sigma_{electrolyte}} + \frac{\tau_{cathode}}{\sigma_{cathode}} \tag{14}$$

where τ is the thickness and σ is the electrical conductivity.

The relation between the activation losses and current density is described by a Butler-Volmer equation [47]:

$$i_{loc} = i_0\left[\exp\left(\alpha\frac{n_e F\eta_{act}}{RT}\right) - \exp\left(-(1-\alpha)\frac{n_e F\eta_{act}}{RT}\right)\right] \tag{15}$$

where α is the transfer coefficient (dimensionless) which is conventional to assume symmetric electron transfer in the Butler-Volmer equation, F is Faraday constant, and i_0 is the reference exchange current density which can be described by Equation (16).

$$i_0 = \frac{RT}{n_e F}k_e'' \exp\left(\frac{-E_{a,e}}{RT}\right) \tag{16}$$

2.2.2. Momentum transfer model

Phenomena involving simultaneous flow through both a pure fluid and a porous medium are observed in diverse industrial processes and natural occurrences, which can be described by the Darcy-Brinkman Equation:

$$\nabla\cdot(\rho\vec{u}) = Q_{br} \tag{17}$$

$$\frac{\rho_g}{\varepsilon}\cdot(\nabla\cdot\vec{u})\cdot\frac{\vec{u}}{\varepsilon} - \nabla\Bigg[-p + \frac{\mu_g}{\varepsilon}\left\{\psi - \frac{2}{3}(\nabla\cdot\vec{u})\right\}\Bigg] + \left(\frac{\mu_g}{\kappa} + \beta_F|\vec{u}| + \frac{Q_{br}}{\varepsilon^2}\right)\cdot\vec{u} = F \tag{18}$$

where $\boldsymbol{F}$ is the volume force vector, k is the permeability of the porous medium, u is the velocity, p is the pressure, Ψ is the viscous stress tensor, and Q_{br} is the source term.

The momentum equation in the air and fuel channels can be simplified as:

$$\nabla\cdot(\rho\vec{u}) = 0 \tag{19}$$

$$\rho_g\cdot(\nabla\cdot\vec{u})\cdot\vec{u} - \nabla\left[-p + \mu_g\cdot\left\{\psi - \frac{2}{3}(\nabla\cdot\vec{u})\right\}\right] = F \tag{20}$$

The viscosity and density of gas mixtures depend on the local temperature and mole fractions.

$$\rho_g = \frac{p\cdot\sum x_j\cdot M_j}{RT} \tag{21}$$

$$\mu_j = \sum_{k=1}^{7} b_k\left(\frac{T}{1000}\right)^k \tag{22}$$

$$\mu_g = \sum_i x_j\cdot\mu_j \tag{23}$$

where x_j is the mole fraction of gas-phase species j and b_k is the species dependent parameter.

2.2.3. Mass transfer model

Gas-phase species diffusion occurs through two mechanisms in porous electrodes: Knudsen diffusion, which involves collisions between gas molecules and pore walls, and molecular diffusion, which arises from collisions between different gas molecules. Mass transport within the SOFC occurs through a combination of diffusion and convection. The following equation for mass transport is employed to simulate the steady-state species conveyance within the flow fields and electrodes of the fuel cell.

$$\nabla\left(-\rho\cdot\omega_i\sum D_{eff,ij}\cdot\nabla x_j + (x_j-\omega_j)\frac{\nabla p}{p}\cdot\vec{u} - D_i^T\cdot\frac{\nabla T}{T}\right) + \rho\cdot\vec{u}\cdot\nabla\omega_j = S_i \tag{24}$$

where DT *i*is the thermal diffusion coefficient, ω is the mass fraction and S_i is the primary term of electrochemical reactions. For a multi-component gas mixing system, the molecular diffusion coefficient can be calculated as:

$$D_{ij} = \frac{k_d\cdot T^{1.75}\cdot\left(\frac{1}{M_i}+\frac{1}{M_j}\right)^{0.5}}{p\cdot\left(v_i^{1/3}+v_j^{1/3}\right)^2} \tag{25}$$

where k_d is the reference diffusivity, M_i and v_i are molar mass and diffusion volume respectively.

2.2.4. Heat transfer model

It is assumed that the local temperature of the solid phase and the gas phase in the electrode are the same. The thermal energy equation can be written as:

$$\rho_g\cdot\varepsilon\cdot c_{p,g}\cdot\vec{u}\cdot\nabla T = \nabla\cdot(k_{eff}\nabla T) + Q \tag{26}$$

This assumes that pure heat conduction occurs in the electrolyte layer and interconnector, meaning that there is no convective heat transfer in the part of the equation. In addition, the gas flow rate in the electrode and channel is not zero, and there is convective heat transfer. Equivalent parameters used in porous structures, such as equivalent thermal conductivity, which be calculated as:

$$k_{eff} = \varepsilon\cdot k_g + (1-\varepsilon)\cdot k_s \tag{27}$$

The specific heat for each gas species i and the gas mixture are described by Equation (28) and (29).

$$C_{p,j} = \frac{\sum_{k=1}^{7} a_k\cdot\left(\frac{T}{1000}\right)^k}{M_j} \tag{28}$$

$$C_{p,g} = \sum_i x_j\cdot c_{p,j} \tag{29}$$

The thermal conductivity of each gas phase and of the gas mixture are defined as follows:

Table 2
Material characteristics.

Parameter	Anode	Cathode	Electrolyte	Interconnector
Thermal conductivity ($W{\cdot}m^{-1}K^{-1}$)	11	6	2.7	20
Density ($kg{\cdot}m^{-3}$)	3310	3030	5160	3030
Specific heat ($J{\cdot}kg^{-1}K^{-1}$)	450	430	470	550

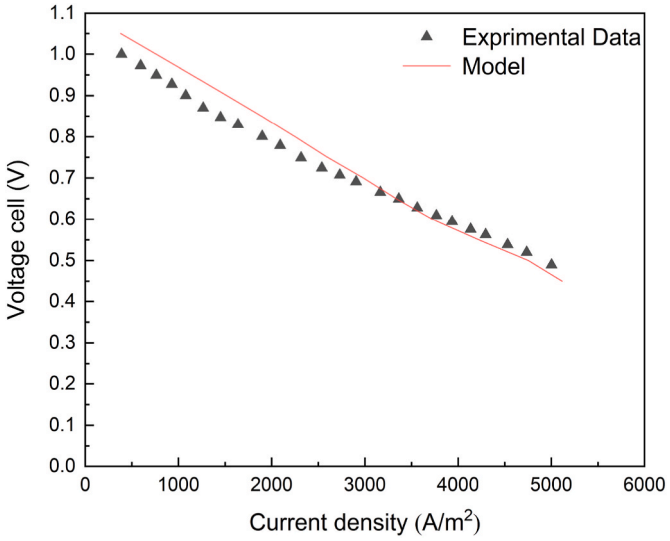

Fig. 3. Polarization curve verification.

$$k_j = 0.01 \cdot \sum_{k=1}^{7} c_k \cdot \left(\frac{T}{1000}\right)^k \tag{30}$$

$$k_g = \sum_i x_j \cdot k_j \tag{31}$$

The source term Q for the thermal energy equation in the anode/cathode layers, arising from the electrochemical reactions, can be expressed as:

$$Q = |i| \cdot \left(\frac{T \cdot |\Delta S_r|}{n_e \cdot F} + |\eta_{act}| + \eta_{conc}\right) + \sum \frac{i^2}{\sigma} \tag{32}$$

2.3. Boundary conditions and material properties

The model in this work is computed by using ANSYS Fluent software. The numerical discretization is implemented using the finite volume method (FVM), with second-order upwind schemes applied to the governing equations for pressure, momentum, and energy. Several assumptions are proposed as follows to simplified model in the simulation:

(1) The simulation assumes steady-state conditions;
(2) The heat radiation effect is neglected;
(3) The fuel and air are considered as ideal gases;
(4) The influence of contact resistance at the interface of the cell is ignored;
(5) Isotropic properties are considered for the electrodes and electrolyte materials.

The material physical properties are summarized in Table 2 [36]. The operates with anode and cathode inlet temperatures maintained at 873.15 K and 1073.15 K, respectively [36]. The inlet is set as a velocity inlet, with the anode inlet velocity at 0.8 m/s and the cathode inlet velocity at 1.7 m/s. H_2 and H_2O mole fractions at the anode inlet are 0.8

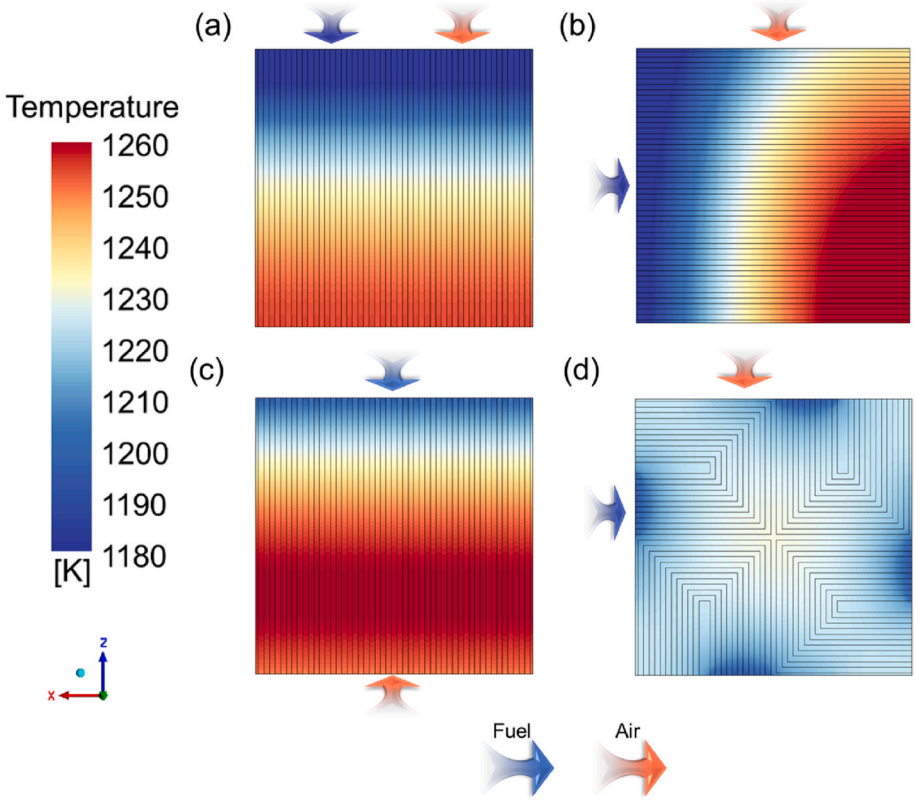

Fig. 4. Temperature distribution of various flow fields at 5000A/m^2: (a) Co-flow field; (b) Cross-flow field; (c)Counter-flow field; (d) Loop-flow field.

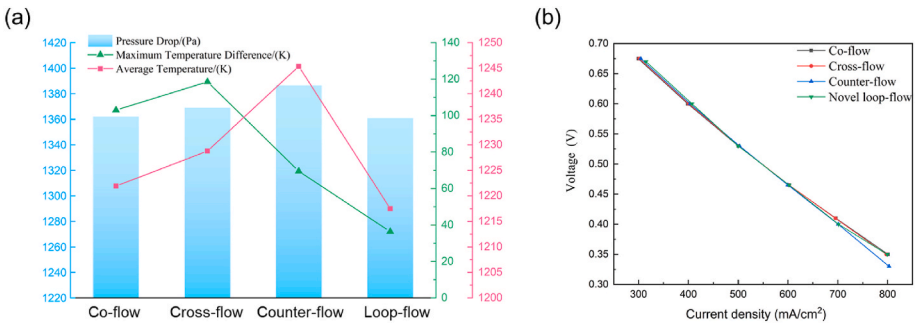

Fig. 5. (a) The pressure drop, maximum temperature difference and average electrolyte temperature for various flow fields; (b) Polarization curve.

and 0.2, while O_2 and N_2 fractions at the cathode inlet are 0.21 and 0.79. The outlet is configured as a pressure outlet with the pressure set to ambient condition. The open-circuit voltage is set to 1.1V and the operating pressure is set to 1 bar.

Since the number of grids has a substantial impact on both the precision of simulations and the duration of computations, it is crucial to perform grid independence verification on the computational models. The grid independence verification results are presented in the supplementary materials. Based on the results and considering the balance between model accuracy and computational cost, the optimal mesh sizes for four flow fields are selected.

2.4. Model validation

To verify the accuracy of the model established above, we build a simulation model with geometric and material parameters consistent with A. Rava's [47]data, and compare the cell performance (I–V curve) with experimental data. The results are shown in Fig. 3. The simulation results are in excellent agreement with the experimental data.

3. Results and discussion

3.1. Thermal performance analysis

Fig. 4 presents the distinct temperature distribution governed by flow field configurations under the 5000 A/m^2 operation. As can be seen from Fig. 4 (a), for a conventional parallel flow field with co-flow field, sustained exothermic reactions induce monotonic axial temperature escalation, with the temperature of the electrolyte exhibiting flow-aligned progressive rising. Due to the characteristics of the flow direction, the temperature of the electrolyte exhibits a sectorial distribution and increases progressively along the diagonal direction in the cross-flow field. The maximum and minimum temperature are located at opposite ends of the diagonal, resulting in the extreme temperature uneven. Within the counter-flow field, the high temperature of oxygen at the inlet causes heat accumulation on the cathode side, leading to a higher electrolyte temperature near the oxygen inlet. In addition, the counter-flow field exhibits better temperature distribution uniformity compared to co-flow and cross-flow fields. Among them, the novel loop-flow field exhibits the most uniform temperature distribution. Except for a pronounced temperature variation zone exclusively at the inlet, the overall performance is better than other flow fields.

It can be seen from Fig. 5 (a) that the maximum temperature difference (TD) of the cross-flow field is the highest, reaching threefold that of the innovative loop-flow field. The innovative loop-flow field significantly diminishes the maximum TD, achieving a substantial reduction of 64.68 % in comparison to the co-flow field and 47.65 % when contrasted with the counter-flow field. Furthermore, the counter-flow field exhibits pronounced thermal accumulation, reflected in its average electrolyte temperature surpassing alternative fields by a considerable margin. While sharing equivalent electrochemical characteristics with the counter-flow (as confirmed by polarization curve alignment in Fig. 5

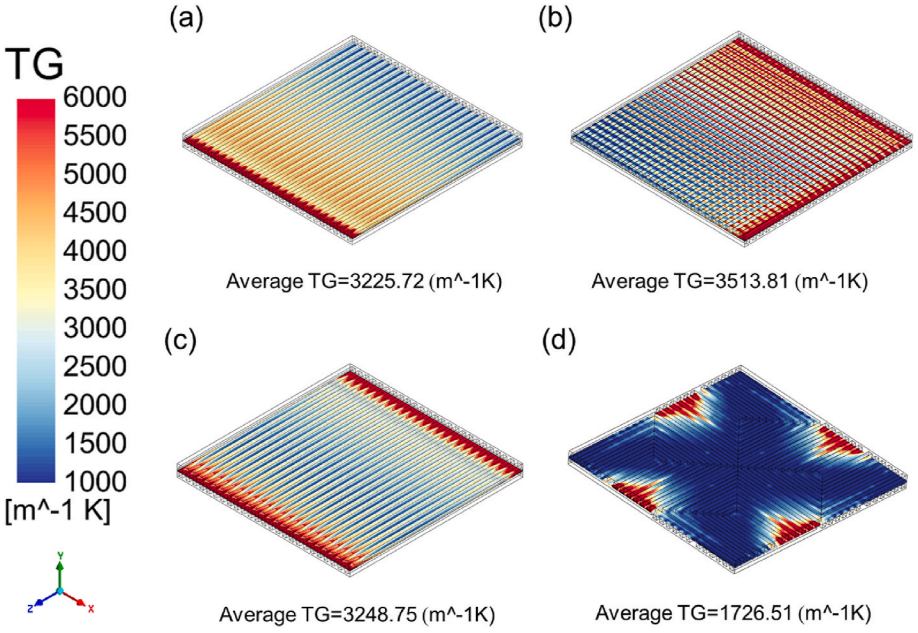

Fig. 6. The temperature gradient of various flow fields at 5000A/m^2: (a) Co-flow field; (b) Cross-flow field; (c)Counter-flow field; (d) Loop-flow field.

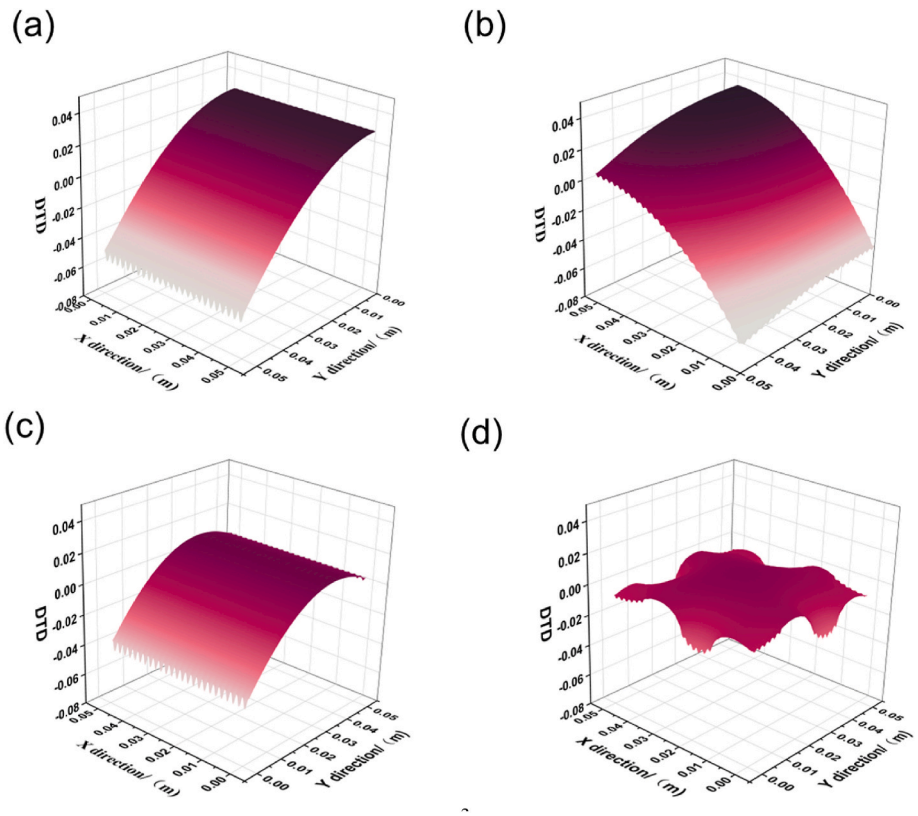

Fig. 7. DTD of various flow fields at 5000A/m^2: (a) Co-flow field; (b) Cross-flow field; (c) Counter-flow field; (d) Loop-flow field.

Table 3
The maximum and minimum values of DTD.

Channel type	Co-flow	Cross-flow	Counter-flow	Loop-flow
Maximum DTD	0.0267	0.0341	0.0128	0.0073
Minimum DTD	−0.0575	−0.0623	−0.0430	−0.0225

(b)), the novel loop-flow field achieves a 28K reduction in mean operating temperature as visualized in Fig. 5(a). This demonstrates the loop-flow field optimizes the heat redistribution pathways.

The temperature gradient distribution of the Positive electrolyte negative (PEN) structure in SOFC is shown in Fig. 6. Thermal gradients within the PEN multilayered structure of SOFCs induce spatially varying thermal expansion, a critical factor driving interfacial delamination and crack nucleation [46,49,50]. Consequently, quantifying both the magnitude and spatial evolution of temperature gradients is essential to assess the thermal characteristics of SOFC. As illustrated in Fig. 6 (b), the average temperature gradient of the flow field with cross-flow distribution is the highest, manifesting a distinctive sectorial distribution pattern. The novel loop-flow field has the lowest average temperature gradient, marking a 50.86 % reduction when compared to the distribution of the cross-flow field. The region with higher temperature gradient mainly exists at the inlet. The temperature gradient at the cathode entrance is significantly higher than that on the anode side, as evidenced by the temperature distribution profile.

In order to reflect the superior temperature distribution uniformity of the innovative loop-flow field, Dimensionless temperature difference (DTD) is calculated as follows:

$$DTD = \frac{T - \overline{T}}{\overline{T}} \tag{33}$$

For the co-flow field, the flow is arranged in an array along the X direction, resulting in a uniform temperature distribution along this direction. However, the DTD increases significantly along the Y direction, leading to an extremely uneven temperature distribution, as shown in Fig. 7 (a). The maximum absolute value of DTD is reduced by 63.88 % when the cross-flow field is changed to innovative loop-flow field as shown in Table 3. The counter-flow field shares similar X direction thermal behavior with co-flow field, but the DTD manifests a tendency to decline initially and subsequently rise in the Y direction. The loop-flow field design achieves uniform thermal distribution along the centerline, eliminating the localized hotspots. The maximum absolute value of DTD is reduced by 60.87 % and 47.67 % compared to co-flow and counter-flow.

3.2. Flow performance analysis

3.2.1. The oxygen and hydrogen mole fraction distribution

Fig. 8 shows the distribution of oxygen mole fraction at the cathode electrode and hydrogen mole fraction at the anode electrode, respectively. Analysis of Fig. 8(a)–(c) reveals a progressive decline in hydrogen concentration following the fuel flow direction. The region of elevated hydrogen concentration expands and is distributed at the fuel intakes on four sides as shown in Fig. 8 (d). The oxygen concentration distribution in co-flow, cross-flow, and counter-flow fields is similar, with the concentration gradually decreasing along the flow direction. Between the inlet and outlet sides, there exists a region of locally low oxygen concentration. However, the area of high oxygen concentration also expands significantly in Fig. 8 (h).

3.2.2. Pressure

From Fig. 5, it can be observed that the counter-flow distribution experiences the highest pressure drop. However, the difference in pressure drops when compared to other flow fields is relatively small. Fig. 9 shows the pressure distribution of the cathode gas channel. The pressure drop in the loop-flow field is nearly the same as that in the co-flow field. Although the serpentine design increases flow resistance and

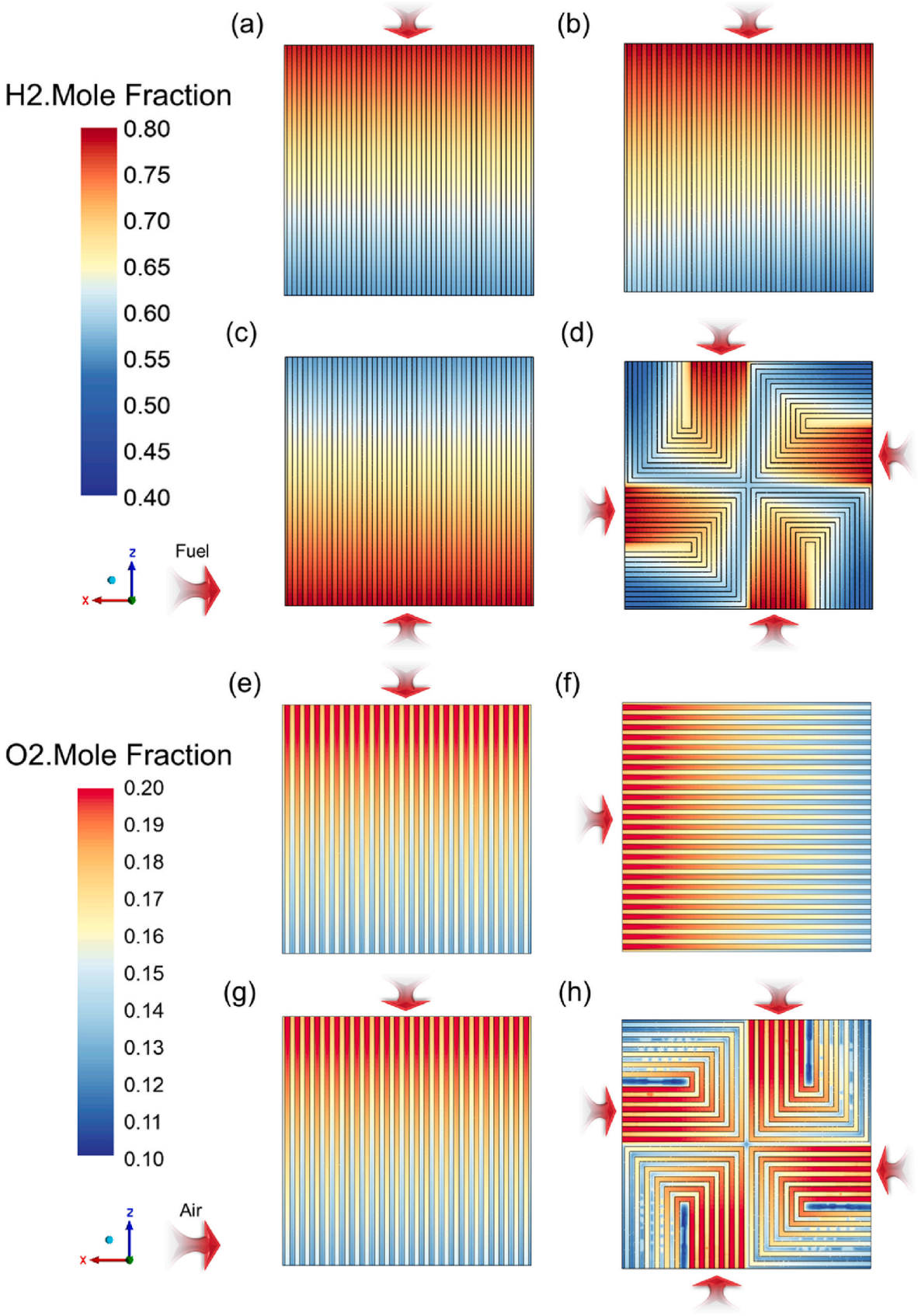

Fig. 8. The distribution of hydrogen mole fraction for various flow fields at 5000A/m^2: (a) Co-flow field; (b) Cross-flow field; (c)Counter-flow field; (d) Loop-flow field. The distribution of oxygen mole fraction for various flow fields at 5000A/m^2: (e) Co-flow field; (f) Cross-flow field; (g)Counter-flow field; (h) Loop-flow field.

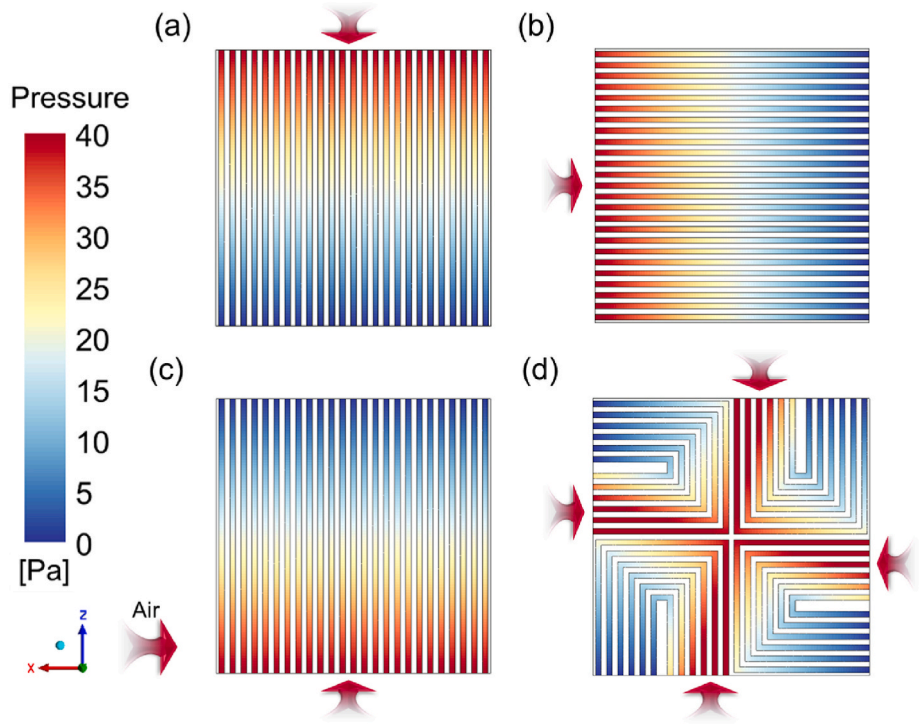

Fig. 9. The pressure distribution of various flow fields at 5000A/m^2: (a) Co-flow field; (b) Cross-flow field; (c) Counter-flow field; (d) Loop-flow field.

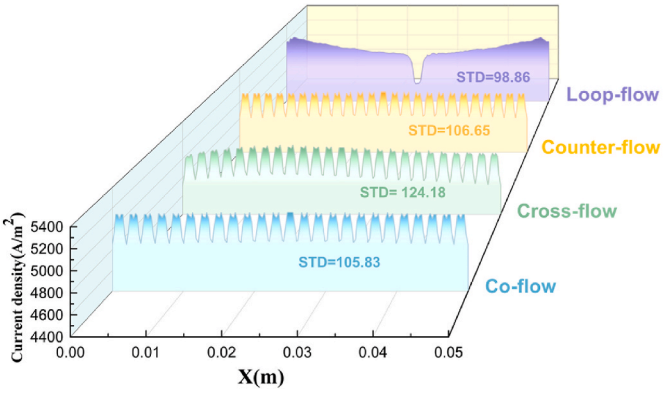

Fig. 10. Current density distribution in various flow fields.

leads to a rise in pressure drop, the shorter channel length effectively offsets this effect.

3.3. Electrical performance analysis

Fig. 10 shows the current density distribution of the vertical line positioned at the center of the electrolyte's mid-thickness cross-section under various flow fields. The result shows that the cross-flow configurations exhibit the lowest homogeneity current density distribution, with a standard deviation (STD) of 124.18. Furthermore, the distribution of current density is similar between co-flow field and counter-flow field, with the STD being almost identical. The flow field of the novel loop-flow field has the lowest STD. Despite the presence of a "trough region" in the central area, the current density distribution in other regions remains highly uniform. The uniformity of current density distribution implies a uniform distribution of electrochemical reaction heat and joule heat, thereby enabling its thermal properties to exhibit a more homogeneous distribution.

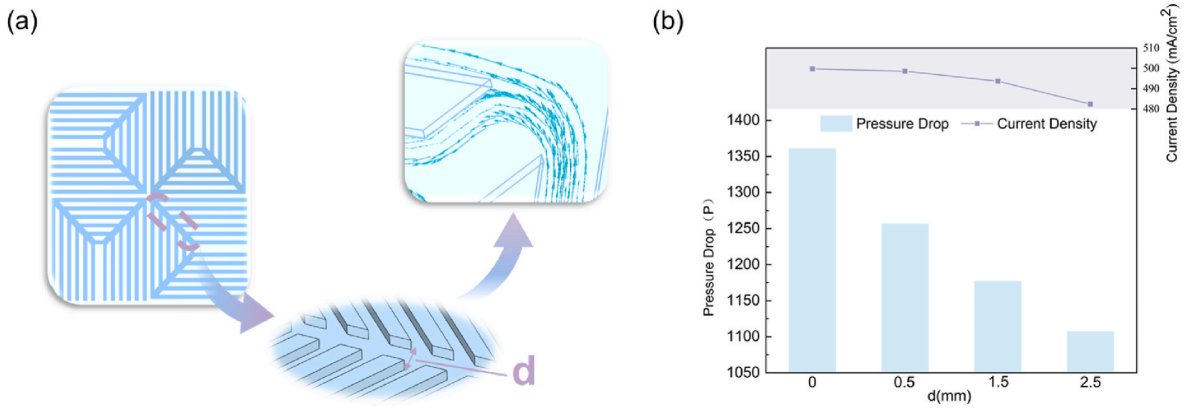

Fig. 11. (a) Branch channels; (b) The current density and pressure drop at 0.53V.

Table 4
The value of PI for different channel widths.

d (mm)	0	0.5	1.5	2.5
Current density (mA/cm2)	499.782	498.661	493.785	482.489
Pressure drop (pa)	1360.8	1256.64	1176.96	1106.88
PI	363.702	372.997	376.089	371.801

3.4. Optimization of the novel loop-flow field

From the above discussion, it can be seen that the novel loop-flow arrangement has significantly improved in thermal characteristics, but the pressure drop has not shown a substantial improvement. Therefore, this subsection focuses on addressing the pressure drop issue. The aim of optimizing the loop structure is to reduce the pressure drop while maintaining uniform temperature distribution and maximizing electrochemical performance. In order to reduce the flow pressure drop, we can adopt methods such as gradually expanding channels, shortening flow paths, and branching channels [51]. According to the feasibility, we incorporate the branch channel into the loop-flow field as shown in Fig. 11 (a), and the effects of four different branch channel widths of 0 mm, 0.5 mm, 1.5 mm and 2.5 mm on the performance are discussed in detail.

Fig.11 (b) shows the current density and pressure drop under the operating voltage of 0.53V. With the increase of channel width, the pressure drop also decrease. As the branch channel width increases, the area of high pressure diminishes progressively. It can also be observed that the electrochemical performance decreases with the increase of the channel width, because when the fluid enters the branch region, the flow space expands, causing a change in the flow rate. As a result, the mass transfer rate between the electrolyte surface and the electrode is affected, leading to a reduction in current density.

In order to measure the electrical performance and pressure drop, we define an indicator, as shown below:

$$PerformanceIndex = \alpha \times CurrentDensity - \beta \times \Pr essureDrop \quad (34)$$

Where α is the weight coefficient of current density and β is the weight coefficient of pressure drop. To ensure that current density and voltage drop contributions to PI are in a comparable range (same order of magnitude), we define $\alpha = 1$ and $\beta = 0.1$. The calculated Performance Index (PI) values are shown in the following Table 4. When the channel width is 1.5 mm, the PI value is the highest, and the current density is only reduced by 1.2 % while the pressure drop is significantly reduced by 11.1 %. Furthermore, the thermal characteristics are also enhanced with the use of branch channels.

Fig. 12 shows the temperature distribution under different channel widths. With the increase of channel width, the average temperature decreases, and the area of the central high-temperature region significantly reduces, while the low-temperature area at the four sides expands notably. To some extent, it can be attributed to the fact that an increase in the width of the branch channels promotes a more homogeneous distribution of the gas, leading to a more homogeneous distribution of electrochemical heat.

4. Conclusions

In this study, in order to improve the temperature uniformity and stability of SOFC, an innovative type of flow field is proposed and numerically simulated. The results show that the proposed flow field configuration demonstrates superior thermal management performance compared to the traditional flow fields. Furthermore, branch channels are incorporated to reduce the pressure drop and enhance efficiency, with an investigation into the effects of different channel widths. The results can be summarized as follows:

(1) The maximum TD of the innovative loop-flow is reduced by 64.68 % compared with the co-flow field, 69.3 % compared with the cross-flow flow field, and 47.65 % compared with the counter-flow flow field.
(2) The average temperature gradient of the loop-flow field is the lowest, reduced by 50.86 % compared to the highest value observed in the cross-flow field.
(3) The maximum absolute value of DTD of the loop-flow field is 60.87 %, 63.88 % and 47.67 % lower than that of co-flow, cross-flow and counter-flow, respectively.

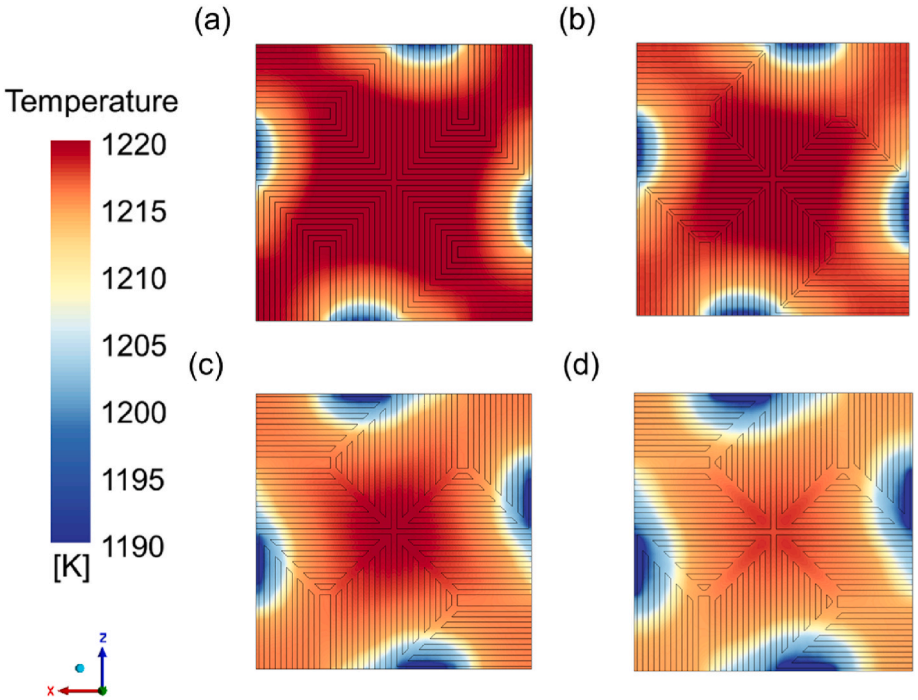

Fig. 12. The temperature distribution of various channel widths at 5000A/m^2: (a) d = 0 mm; (b) d = 0.5 mm; (c) d = 1.5 mm; (d) d = 2.5 mm.

(4) When the branch channel width is set to 1.5 mm, the performance evaluation index PI reaches its maximum value. In comparison with the configuration lacking branch channels, the current density exhibits a slight decrease of 1.2 %, whereas the pressure drop is significantly reduced by 11.1 %. Furthermore, the thermal performance is notably enhanced, as evidenced by the average temperature is reduced.

CRediT authorship contribution statement

Jiaxuan Wu: Writing – review & editing, Writing – original draft, Validation, Methodology, Data curation, Conceptualization. **Jingjin Hu:** Writing – review & editing, Methodology, Data curation. **Zhengkai Tu:** Writing – review & editing. **Run Hu:** Writing – review & editing, Writing – original draft, Supervision, Conceptualization.

Declaration of competing interest

The authors declare that they have no known competing financial interests or personal relationships that could have appeared to influence the work reported in this paper.

Acknowledgments

The authors would like to acknowledge the financial support from the National Key Research and Development Program of China (2024YFB4104701).

Appendix A. Supplementary data

Supplementary data to this article can be found online at https://doi.org/10.1016/j.ijhydene.2025.04.463.

References

[1] Zhu S, Liu X, Wang X, Zhao Q, Shao M. Some remaining puzzles in hydrogen electrocatalysis mechanisms on platinum surfaces. Joule 2024;8(7):1890–918.
[2] Yue M, Lambert H, Pahon E, Roche R, Jemei S, Hissel D. Hydrogen energy systems: a critical review of technologies, applications, trends and challenges. Renew Sustain Energy Rev 2021;146:111180.
[3] Meda US, Rajyaguru YV, Pandey A. Generation of green hydrogen using self-sustained regenerative fuel cells: opportunities and challenges. Int J Hydrogen Energy 2023;48(73):28289–314.
[4] Hyun J, Kim H-T. Powering the hydrogen future: current status and challenges of anion exchange membrane fuel cells. Energy Environ Sci 2023;16(12):5633–62.
[5] Singh M, Zappa D, Comini E. Solid oxide fuel cell: decade of progress, future perspectives and challenges. Int J Hydrogen Energy 2021;46(54):27643–74.
[6] Yi B, Huo C, Xue D, Zou H, Yan Y, Li G. A numerical study of the performance of solid oxide fuel cell with bi-layer interconnector. Int J Hydrogen Energy 2024;87:1233–44.
[7] Jiang J, Zhou R, Xu H, Wang H, Wu P, Wang Z, Li J. Optimal sizing, operation strategy and case study of a grid-connected solid oxide fuel cell microgrid. Appl Energy 2022;307:118214.
[8] Pan Z, Shen J, Wang J, Xu X, Chan WP, Liu S, Zhou Y, Yan Z, Jiao Z, Lim T-T, Zhong Z. Thermodynamic analyses of a standalone diesel-fueled distributed power generation system based on solid oxide fuel cells. Appl Energy 2022;308:118396.
[9] Hou J, Yang M, Zhang J. Active and passive fuel recirculation for solid oxide and proton exchange membrane fuel cells. Renew Energy 2020;155:1355–71.
[10] Wu X-l, Xu Y-w, Li D, Zheng Y, Li J, Sorrentino M, Yu Y, Wan X, Hu L, Zou C, Li X. Afterburner temperature safety assessment for solid oxide fuel cell system based on computational fluid dynamics. J Power Sources 2021;496:229837.
[11] Guo M, Li Z, Yue Z, Lin Z, Jiang S. Long-term thermo-mechanical performance evolution of a 15-cell solid oxide fuel cell stack. Int J Hydrogen Energy 2024;62:1258–72.
[12] Aguiar P, Adjiman CS, Brandon NP. Anode-supported intermediate-temperature direct internal reforming solid oxide fuel cell. J Power Sources 2005;147(1–2):136–47.
[13] Fan Y, Jian J, Zhang X, Mei S, Zhu Y, Jiang W, Wang S. Experimental investigation of temperature distribution in solid oxide fuel cells. Int J Hydrogen Energy 2024;79:850–63.
[14] Zeng Z, Qian Y, Zhang Y, Hao C, Dan D, Zhuge W. A review of heat transfer and thermal management methods for temperature gradient reduction in solid oxide fuel cell (SOFC) stacks. Appl Energy 2020;280:115899.
[15] Liu L, Kim G-Y, Chandra A. Modeling of thermal stresses and lifetime prediction of planar solid oxide fuel cell under thermal cycling conditions. J Power Sources 2010;195(8):2310–8.
[16] Xu M, Li TS, Yang M, Andersson M, Fransson I, Larsson T, Sundén B. Modeling of an anode supported solid oxide fuel cell focusing on thermal stresses. Int J Hydrogen Energy 2016;41(33):14927–40.
[17] Wang W, Liu J, Serbin S, Chen D, Zhou H. Thermal stress analysis for a typical planar anode-supported fuel cell stack. Sustain Energy Technol Assessments 2022;54:102891.
[18] Chiang L-K, Liu H-C, Shiu Y-H, Lee C-H, Lee R-Y. Thermo-electrochemical and thermal stress analysis for an anode-supported SOFC cell. Renew Energy 2008;33(12):2580–8.
[19] Miao X-Y, Rizvandi OB, Navasa M, Frandsen HL. Modelling of local mechanical failures in solid oxide cell stacks. Appl Energy 2021;293:116901.
[20] Saied M, Ahmed K, Nemat-Alla M, Ahmed M, El-Sebaie M. Performance study of solid oxide fuel cell with various flow field designs: numerical study. Int J Hydrogen Energy 2018;43(45):20931–46.
[21] Huang CM, Shy SS, Lee CH. On flow uniformity in various interconnects and its influence to cell performance of planar SOFC. J Power Sources 2008;183(1):205–13.
[22] Fu Q, Li Z, Wei W, Liu F, Xu X, Liu Z. Performance enhancement of planar solid oxide fuel cell using a novel interconnector design. Int J Hydrogen Energy 2021;46(41):21634–56.
[23] Kong W, Han Z, Lu S, Gao X, Wang X. A novel interconnector design of SOFC. Int J Hydrogen Energy 2020;45(39):20329–38.
[24] Yan M, Fu P, Li X, Zeng M, Wang Q. Mass transfer enhancement of a spiral-like interconnector for planar solid oxide fuel cells. Appl Energy 2015;160:954–64.
[25] Liu Y, Xu Y, Liu J, Xiang M, Sun B, Ya Y, Guo Z, Cheng X. Effects of bipolar plate flow channel configuration on thermal-electric performance of direct ammonia solid oxide fuel cell: Part I - numerical study of channel section geometry. Int J Hydrogen Energy 2024;50:765–85.
[26] Xia L, Khosravi A, Han M, Sun L. Artificial intelligence based structural optimization of solid oxide fuel cell with three-dimensional reticulated trapezoidal flow field. Int J Hydrogen Energy 2023;48(72):28131–49.
[27] Hao C, Zeng Z, Zhao B, Qian Y, Zhuge W, Wang Y, Shi Y, Zhang Y. Local heat generation management for temperature gradient reduction in tubular solid oxide fuel cells. Appl Therm Eng 2022;211:118453.
[28] Fu L, Liu H, Liu J, Hua Z, Lin H. Research on the effect of connected cable-type channel structure and flow field arrangement on the performance of SOFC. Int J Hydrogen Energy 2024;78:169–79.
[29] Chen D, Zhu Y, Han S, Anatoly L, Andrey M, Lu L. Investigate the effect of a parallel-cylindrical flow field on the solid oxide fuel cell stack performance by 3D multiphysics simulating. J Energy Storage 2023;60:106587.
[30] Oni TO. CFD study of behavior of transition flow in distinct tubes of miscellaneous tape insertions. HighTech and Innovation Journal 2022;3(2):130–9.
[31] Alrwashdeh SS, Ammari H, Madanat MA, Al-Falahat AaM. The effect of heat exchanger design on heat transfer rate and temperature distribution. Emerging Science Journal 2022;6(1):128–37.
[32] Chen D, Zeng Q, Su S, Bi W, Ren Z. Geometric optimization of a 10-cell modular planar solid oxide fuel cell stack manifold. Appl Energy 2013;112:1100–7.
[33] Fardadi M, McLarty DF, Jabbari F. Investigation of thermal control for different SOFC flow geometries. Appl Energy 2016;178:43–55.
[34] Lee HL, Han NG, Kim MS, Kim YS, Kim DK. Studies on the effect of flow configuration on the temperature distribution and performance in a high current density region of solid oxide fuel cell. Appl Therm Eng 2022;206:118120.
[35] Lu P, Wei S, Du Z, Ma W, Ni S. Analysis and comparison of multi-physics fields for different flow field configurations in SOFC. Int J Heat Mass Tran 2024;229:125708.
[36] Gong C, Luo X, Tu Z, Chan SH. A novel flow channel design to achieve high temperature homogenization in solid oxide fuel cell. Int J Hydrogen Energy 2024;52:442–53.
[37] Zhang W, Kuang X, Zhang W, Yan D, Jia L. Flow field optimization for performance enhancement of planar solid oxide fuel cells. Int J Hydrogen Energy 2024;62:1171–82.
[38] Chen D, Xu Y, Tade MO, Shao Z. General regulation of air flow distribution characteristics within planar solid oxide fuel cell stacks. ACS Energy Lett 2017;2(2):319–26.
[39] Tan WC, Iwai H, Kishimoto M, Yoshida H. Quasi-three-dimensional numerical simulation of a solid oxide fuel cell short stack: effects of flow configurations including air-flow alternation. J Power Sources 2018;400:135–46.
[40] Zhao C, Yang J, Zhang T, Yan D, Pu J, Chi B, Li J. Numerical modeling of manifold design and flow uniformity analysis of an external manifold solid oxide fuel cell stack. Int J Hydrogen Energy 2020;45(28):14440–51.
[41] Kim YJ, Jung WN, Yu JH, Kim HJ, Yun KS, Kang DG, Lee MC. Design and analysis of SOFC stack with different types of external manifolds. Int J Hydrogen Energy 2020;45(53):29143–54.
[42] Bi W, Chen D, Lin Z. A key geometric parameter for the flow uniformity in planar solid oxide fuel cell stacks. Int J Hydrogen Energy 2009;34(9):3873–84.
[43] Yang J, Yan D, Huang W, Li J, Pu J, Chi B, Jian L. Improvement on durability and thermal cycle performance for solid oxide fuel cell stack with external manifold structure. Energy 2018;149:903–13.
[44] Chen X, Ji Y, Yang J, Yan D, Jia L, Han X, Wu K, Li J. Flow uniformity analysis and optimization of a 60-cell external manifold solid oxide cell stack with bottom-accesses. Int J Hydrogen Energy 2023;48(82):32056–67.
[45] Gong C, Luo X, Tu Z. Thermal management of bypass valves for temperature difference elimination in a 5 kW multi-stack solid oxide fuel cell system. Appl Therm Eng 2023;229:120590.

[46] Gong C, Tu Z, Hwa Chan S. A novel flow field design with flow re-distribution for advanced thermal management in Solid oxide fuel cell. Appl Energy 2023;331:120364.
[47] Khazaee I, Rava A. Numerical simulation of the performance of solid oxide fuel cell with different flow channel geometries. Energy 2017;119:235–44.
[48] Patcharavorachot Y, Arpornwichanop A, Chuachuensuk A. Electrochemical study of a planar solid oxide fuel cell: role of support structures. J Power Sources 2008;177(2):254–61.
[49] Clague R, Marquis AJ, Brandon NP. Finite element and analytical stress analysis of a solid oxide fuel cell. J Power Sources 2012;210:224–32.
[50] Mehdizadeh Chellehbari Y, Adavi K, Sayyad Amin J, Zendehboudi S. A numerical simulation to effectively assess impacts of flow channels characteristics on solid oxide fuel cell performance. Energy Convers Manag 2021;244:114280.
[51] Chai Y, Qu D, Fan L, Zheng Y, Yang F. A double-spiral flow channel of vanadium redox flow batteries for enhancing mass transfer and reducing pressure drop. J Energy Storage 2024;78:110278.